GEOPHYSICS, VOL. 83, NO. 4 (JULY-AUGUST 2018); P. T195–T207, 19 FIGS.
10.1190/GEO2017-0536.1

How to adapt numerical simulation of wave propagation and ultrasonic laboratory experiments to be comparable — A case study for a complex topographic model

Bence Solymosi[1], Nathalie Favretto-Cristini[1], Vadim Monteiller[1], Dimitri Komatitsch[1], Paul Cristini[1], Børge Arntsen[2], and Bjørn Ursin[2]

ABSTRACT

Numerical methods are widely used in seismic exploration to simulate wave propagation; however, the algorithms are based on various assumptions. The accuracy of numerical simulations is of particular interest in the case of realistic geologic setups. The direct comparison of numerical results can have limitations, and an alternative approach can be the comparison of synthetic results with experimental data, obtained for a small-scale physical model in laboratory conditions. Laboratory experiments are repeatable and provide high-quality data for a known configuration. We have developed a possible workflow to adapt the numerical simulations and the laboratory experiments to each other, such that the two can be easily compared with high accuracy. The model is immersed in a water tank, and a conventional pulse-echo technique is used to collect the reflection data in zero-offset and offset configurations. We use a spectral-element method for the numerical modeling. The model geometry is implemented using a nonstructured mesh, and the computational cost can be optimized using larger elements and higher-order basis functions. The real source transducer characteristics are implemented based on a new approach: laboratory characterization of the impulse response, followed by an inversion step to obtain a numerically equivalent source. The comparison of the zero-offset synthetic and laboratory results reveals an excellent fit in terms of arrival time, phase, and amplitude. Minor amplitude mismatches may be attributed to the noise recorded in the laboratory data and to the possible inaccuracy of the proposed source implementation. Comparison of the simulated and laboratory offset traces also exhibits a good fit in general, but with significantly less accuracy for some arrivals than in the zero-offset case. This can be mainly attributed to the inaccuracies of the transducer positions during the laboratory measurements combined with the strong topography of the model.

INTRODUCTION

Numerical simulation of seismic-wave propagation is widely used in environmental and industrial applications for subsurface evaluation in seismic exploration (e.g., for survey design, data processing, and interpretation; Robertsson et al., 2007). Simulation is also a core tool of seismic imaging and inversion (Virieux et al., 2011). Conventional methods (e.g., ray tracing, Kirchhoff integral, and finite-difference methods), widely used in seismic exploration, are efficient to simulate realistic wavefields in environments with simple structures and slowly varying material properties. However, difficulties arise for environments with large and rapid structural changes, due to shadow zones and (multiple) diffractions. Thus, different methods have been developed to improve seismic modeling in realistic geologic environments, including steeply dipping faults, curved interfaces, and salt bodies (e.g., Mittet, 2017). Before real applications, new methods are typically tested against other numerical methods using synthetic configurations. Several projects have focused on the comparison and validation of different numerical results (e.g., Igel et al., 2000; Moczo et al., 2006; Fehler and Keliher, 2011; Chaljub et al., 2015). Because each numerical algorithm is based on mathematical or physical assumptions, their direct

Manuscript received by the Editor 17 August 2017; revised manuscript received 16 February 2018; published ahead of production 16 April 2018; published online 8 June 2018.
[1]Aix-Marseille University, CNRS, Centrale Marseille, LMA, France. E-mail: solymosi@lma.cnrs-mrs.fr; favretto@lma.cnrs-mrs.fr; monteiller@lma.cnrs-mrs.fr; komatitsch@lma.cnrs-mrs.fr; cristini@lma.cnrs-mrs.fr.
[2]Norwegian University of Science and Technology, Trondheim, Norway. E-mail: borge.arntsen@ntnu.no; bjorn.ursin@ntnu.no.

comparison for realistic and complex models can have limitations because it can be difficult to determine the one that gives the best approximation of a physically unknown solution. Therefore, there is strong interest in using physical data sets to benchmark synthetic results. However, because in real life the subsurface of the earth is never accurately known, the synthetic results cannot be directly compared with any seismic or seismological data set from real measurements.

An alternative approach to test and validate the performance of numerical methods in realistic cases can be the comparison of synthetic results with experimental data, obtained for a small-scale physical model in laboratory conditions. This implicitly assumes that the scaled physical mechanisms are identical to those at seismic scale (Ebrom and McDonald, 1994), and this assumption is fulfilled in the case of the linear wave equation. Considered as obsolete in the 1990s essentially due to the drastic increase in computing capacities, laboratory experiments have recently been reintroduced into the ideas-to-applications pipeline. The laboratory can be considered as a half-way point between numerical modeling and field observations. Indeed, laboratory experiments are repeatable, more controllable than real seismic surveys, versatile in terms of acquisition setup, and provide high-quality data for a known configuration. Furthermore, similar to real seismic acquisitions and unlike some numerical data, laboratory measurements contain random and signal-generated noise, multiples, mode conversions, and uncertainties due to position inaccuracies. Because these sources of noise and uncertainties can be better assessed than in the case of field data sets, laboratory experiments also provide higher fidelity data than real seismic surveys. Therefore, laboratory experiments are a valuable tool to validate numerical simulations against real physical data sets.

Initially, small-scale physical modeling was extensively developed for a better understanding of wave propagation phenomena (e.g., Wapenaar and Berkhout, 1987; Pant et al., 1992) and for the validation of theoretical predictions (Favretto-Anrès and Rabau, 1997). Laboratory experiments are still used nowadays to investigate physics that is not sufficiently understood to be numerically modeled with confidence (Cooper et al., 2010; Stewart et al., 2012; Ekanem et al., 2013; Xu et al., 2016; Chang et al., 2017). Data from laboratory experiments are also used as input to inverse problems (Favretto-Anrès and Sessarego, 1999; Pratt, 1999; Bretaudeau et al., 2013; Chai et al., 2015), to test new data processing algorithms (Campman et al., 2005), and in time-lapse 3D studies (Sherlock et al., 2000). More recently, small-scale modeling approaches have been developed as tools to validate numerical modeling and seismic-imaging methods in the context of onshore and offshore seismics (Bretaudeau et al., 2011; Favretto-Cristini et al., 2014; Tantsereva et al., 2014a, 2014b). In particular, Tantsereva et al. (2014a) evaluate the ability of a 3D discretized Kirchhoff integral method (DKIM) to accurately simulate complex diffractions using a zero-offset laboratory data set, measured for a small-scale model with strong topography, immersed in a water tank. Comparisons of numerical and laboratory data sets showed that the DKIM could correctly reproduce the wavefield, except in the vicinity of secondary shadow boundaries created by the interaction of the edges of the topographic structures. As a follow-up of the work of Tantsereva et al. (2014a), Favretto-Cristini et al. (2017) quantitatively analyze the effect of multiple scattering and surface curvature on the wavefield to define the cases in which these effects may be neglected in the numerical modeling without a significant loss of accuracy. These works clearly show the importance of laboratory data sets as part of the benchmarking options for numerical algorithms.

An efficient benchmarking procedure requires a carefully chosen and jointly adapted approach to the laboratory experiments and the numerical modeling. On the one hand, the numerical tools must be adapted to the experimental configuration (e.g., implementing the real source characteristics, material properties, and acquisition conditions). On the other hand, the laboratory experiments have to be carried out in accordance with the capabilities of the numerical tools (e.g., choosing the acquisition geometry such that the future computational cost is the lowest possible). In addition, experimental uncertainties must be identified, to be subsequently minimized as much as possible, and numerical simulations may also contribute to it.

The goal of this paper is to address the above challenges by providing a possible way to adapt the numerical simulations and the laboratory experiments such that the two can be easily compared with high accuracy. To achieve this goal, we resorted to spectral-element modeling (SEM) as a full-wave method, which is not based on strong underlying assumptions (such as, for example, the DKIM). SEM also becomes more and more popular with time in the seismic community because it is well-suited for high-performance computing (Komatitsch et al., 2003). Because it combines the accuracy of a pseudo-spectral method with the flexibility of a finite-element method, SEM allows for handling of complex geometries by using a nonstructured mesh and different element sizes in the computational domain (Komatitsch and Tromp, 2002; Oliveira and Seriani, 2011). Because the necessary trade-off between accuracy and computational cost is usually sought after, we are also interested in the ability of SEM to accurately simulate complex 3D wavefields including (multiple) diffractions at the lowest possible computational and man-hour cost. Few papers are devoted to the comparison of SEM with other numerical methods (e.g., Capdeville et al., 2002, 2003; Moczo et al., 2010; De Basabe and Sen, 2014; Chaljub et al., 2015). Pageot et al. (2017) recently compare laboratory and synthetic data sets in an onshore configuration to investigate surface wave propagation and amplitude transformation between two dimensions and three dimensions. But to the best of our knowledge, no paper uses laboratory experiments as reference data sets for comparison in an offshore configuration.

In this paper, we thus compare 3D spectral-element simulations with laboratory measurements in 3D zero-offset and 3D offset offshore reflection configurations for the so-called Marseille-Benchie model. To our knowledge, it is the first time that such a comparison for the general offset case is presented. The Marseille-Benchie model is based on French's model (French, 1974), and it also includes additional structures with steep flanks, sharp edges, corners, and curved interfaces (Tantsereva et al., 2014a). It enhances multiple reflections and diffractions, as well as shadow zones and interactions between different structures. This complexity provides a significant challenge to any numerical method to reproduce the wavefield. The paper is organized as follows: The "Small-scale seismic modeling" section briefly describes the laboratory experiments, i.e., the small-scale model and the experimental setup. The laboratory data sets obtained in zero-offset and offset configurations are also presented, together with their physical interpretations. The "Numerical modeling" section is devoted to a short description of SEM. More importantly, we also discuss in detail the input data/parameters, such as the model geometry, the material properties,

and the characteristics of the source and receiver transducers. In the "Data comparisons" section, we compare the laboratory and numerical data sets, and then we discuss the results in the "Discussion" section.

SMALL-SCALE SEISMIC MODELING

We carried out several laboratory experiments in a water tank, in which wave propagation occurs in small-scale conditions. A scaling factor of 1:20,000 is used to scale down the real-life dimensions of typical seismic setups to the laboratory scale. Hence, an experimental frequency of 500 kHz corresponds to a seismic frequency of 25 Hz, and an experimental distance of 1 mm corresponds to 20 m at seismic scale. Material properties, such as velocity, density, and attenuation are not affected directly by the scaling.

Small-scale geologic model

The Marseille-Benchie model contains various complex topographic features, such as a dome, a truncated dome, a truncated pyramid, and two flat parts separated by a ramp (Figure 1). The model is made of polyvinyl chloride (PVC) and has a size of 600×400 mm, corresponding to 12×8 km at seismic scale. Its thickness varies between 30 and 70 mm, depending on the geometry. The measured material properties of the PVC are $V_P = 2220 \pm 10$ m/s, $V_S = 1050 \pm 10$ m/s, and $\rho = 1412 \pm 17$ kg/m^3. PVC is considered to be homogeneous and isotropic for the frequency range of interest of this work (250–650 kHz). For example, the P- and S-wave velocities were found to be quasi-constant for this frequency range, suggesting a negligible dispersion. Attenuation was measured using the amplitude of the transmitted monochromatic sine waves at different frequencies through different PVC samples of varying thickness. Following the measurements, the attenuation can be transformed into quality factors: $30 < Q_P < 60$ and $27 < Q_S < 31$ for P- and S-waves, respectively. As is known, the measurement of attenuation is one of the most difficult laboratory tasks among all the material property characterizations. According to the measurements and accounting for the uncertainties of this parameter, we consider the PVC to have the same quality factor between 250 and 650 kHz, which is in good agreement with the literature (Favretto-Anrès and Rabau, 1997). For further details on the model, see also Tantsereva et al. (2014a).

Experimental setup

Because our work is concerned with offshore measurements, the model was immersed in a water tank equipped with a computer-controlled acquisition system that allows for accurate positioning of the source and receiver transducers. The water temperature was continuously monitored during the measurements, providing accurate knowledge of the speed of sound waves in water (usually approximately 1480 m/s). Water was considered to have a density of 1000 kg/m^3 and negligible attenuation.

A conventional pulse-echo technique was used to collect reflection data in zero-offset and offset configurations (Figure 1). Zero-offset measurements were performed using a custom-made Imasonic® transducer as the source and the receiver. It has a diameter of 3 mm and was located 180 ± 0.5 mm above the flat part of the model (corresponding to 3.6 km at seismic scale). The source signal generated by this transducer and its associated frequency spectrum for the frequency range of interest of this work is shown in Figure 2. The transducer has a dominant frequency of 500 kHz and a broad-beam radiation pattern because the width of the main lobe is 35° at −3 dB. This radiation pattern allows for a large area to be illuminated and therefore more 3D effects to be captured, e.g., the interaction of waves with multiple topographic features and multiple wave scattering (Favretto-Cristini et al., 2017).

Offset measurements were performed using two transducers, namely, the above-mentioned transducer as the source and an omnidirectional Teledyne Reson® hydrophone as the receiver. Both transducers were located 150 ± 0.5 mm above the flat part of the model. The hydrophone has an active diameter of 4 mm, and its sensitivity is constant between 50 and 800 kHz. The source can be tilted with various angles to illuminate different parts of the model or to enhance some particular effects, such as shadow zones.

Laboratory data sets

We performed acquisitions along the x-lines (Figure 1) with a sampling distance of 0.5 mm (corresponding to 10 m at seismic scale). The collected data set thus consists of numerous parallel

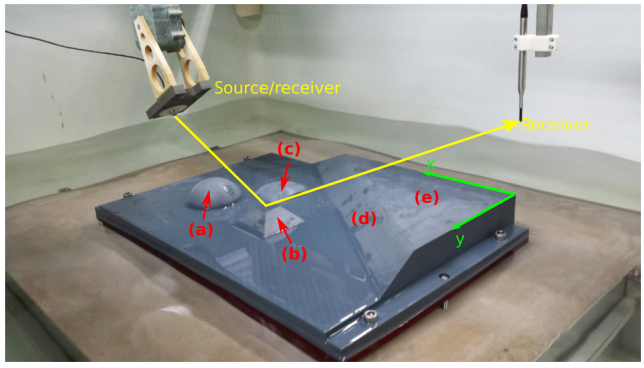

Figure 1. Illustration of the small-scale seismic experiments performed in the water tank. The Marseille-Benchie model contains (a) a dome, (b) a truncated pyramid, (c) a truncated dome, (d) a ramp, and (e) an elevated plateau. The model is illuminated by a piezoelectric transducer (on the left). In the offset configuration, the wavefield is recorded by a hydrophone (on the right).

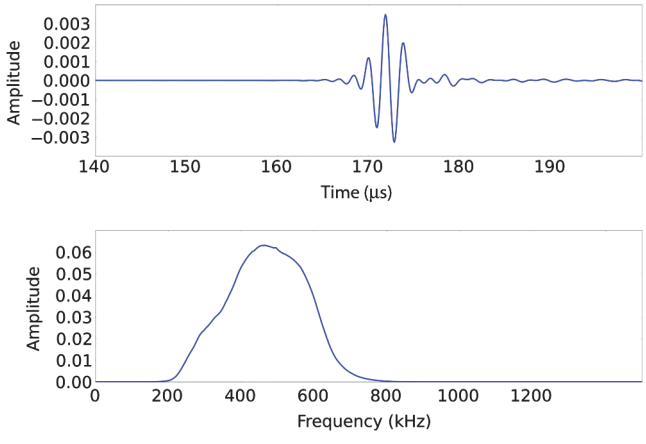

Figure 2. (a) Source signal (filtered between 250 and 650 kHz) generated by the source transducer and recorded by the receiver hydrophone in the opposite position and (b) the associated frequency amplitude spectrum.

profiles, providing a set of reflection data for a dense grid (with receiver spacing of 0.5 mm in both directions). To enhance the signal-to-noise ratio, 256 acquisitions were performed at each grid point and then the individual registrations were stacked. The speed of sound in water was 1485 ± 0.1 and 1484 ± 0.1 m/s for zero-offset and offset measurements, respectively, due to the different water temperatures during the two measurements. The water column above the transducer was always at least 0.6 m, and the tilt angle of the source transducer was 39° for the offset measurements.

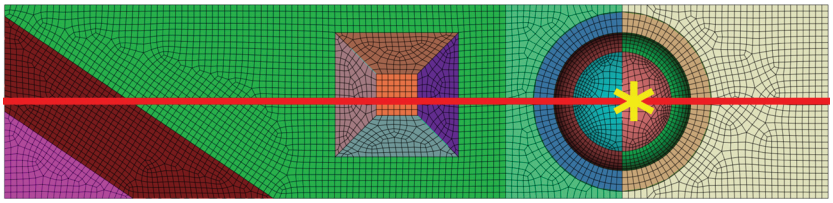

Figure 3. Part of the model used for the numerical simulations with a coarse mesh. The red line denotes the position of the study line discussed in the paper. The yellow asterisk shows the source position for the offset study line. The different colors show the subdomains necessary for the nonstructured meshing.

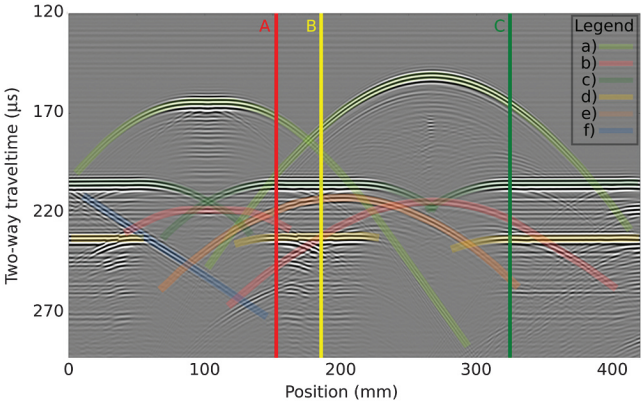

Figure 4. Cross section of the laboratory zero-offset data set, corresponding to the red line in Figure 3. The data were filtered between 250 and 650 kHz. Annotated events: (a and b) The top and bottom of the pyramid and the dome, (c and d) the top and bottom of the flat part, (e) truncated dome, and (f) ramp. The vertical lines denote the zero-offset traces chosen for comparison.

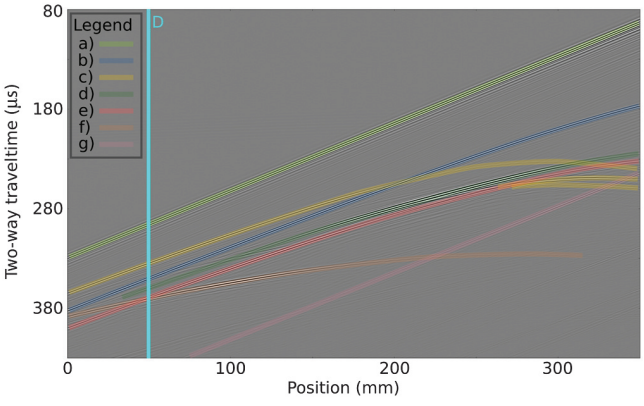

Figure 5. Cross section of the laboratory offset data set (i.e., common-shot gather), corresponding to the red line in Figure 3. The data were filtered between 250 and 650 kHz. Annotated events: (a) direct arrival, (b) dome, (c) pyramid, (d) flat part, (e) truncated dome, (f) ramp, and (g) spurious reflection from the acquisition system. The source position is shown in Figure 3 with the yellow asterisk. The vertical line denotes the offset-trace chosen for comparisons.

For the sake of brevity, we focus only on one line in this paper, located above the full dome, the truncated pyramid, and the ramp (the red line in Figure 3). This acquisition line provides complex diffraction effects, multiple reflections, and arrivals corresponding to curved interfaces. Figure 4 shows the laboratory zero-offset data set for the study line, overlaid by the interpretation of the recorded events. For the sake of clarity, only the main events are shown in Figure 4. Events (a and c) represent the arrivals related to the top surface of the PVC, corresponding to the pyramid and the dome, and to the flat parts, respectively. Event (a) mainly consists of reflections (see the positions between 90 and 115 mm for the pyramid and 95–410 mm for the dome). There are also some diffraction hyperbolas corresponding to the edges of the top surface of the pyramid, for positions less than 90 mm and greater than 115 mm. Moreover, due to the angle of the truncation, there are two smaller hyperbolas in the center of the pyramid, partly overlapping the reflections from the top flat surface of the object. Similar to event (a), event (c) mainly consists of reflections, as well as some diffraction hyperbolas related to the junctions of the pyramid and the dome with the flat part. Events (b and d) correspond to reflections from the bottom of the PVC, below the pyramid and the dome, and below the flat part, respectively. Because Figure 4 is a time section, a classic velocity pull-up effect can be seen in the different arrival times of events (b and d). Indeed, depending on the overburden, reflections from the same horizontal bottom surface of the PVC arrive at different times. Event (e) represents reflections from the small truncated dome (Figure 1). This out-of-plane arrival, which is due to the broad-beam radiation pattern of the source transducer, was not considered during the simulations. Event (f) shows reflections from the ramp, which were partly accounted for during the simulations. Note that the diffractions on the right side of the section after 200 μs and for positions between 300 and 420 mm, are related to the side of the model.

Figure 5 shows the laboratory offset data set (i.e., a common-shot gather) for the study line together with the interpretation of the main events. Event (a) shows the direct arrival from the source, and event (b) shows the reflections from the dome. All the interpretations marked as event (c) correspond to reflections/diffractions from the pyramid. Event (d) illustrates the reflections from the flat part of the PVC. Event (e) is related to reflections from the small truncated dome, and event (f) is related to reflections from the ramp. Event (g) is not related to the model, but to spurious arrivals from the a cquisition system (not considered during the simulations).

NUMERICAL MODELING

We used an SEM for the numerical modeling of the experiments. Following a brief recall of the method, we discuss the strategy used to mesh the model geometry, the numerical implementation of the real transducer characteristics, and the preliminary numerical calibration of the material properties.

Recall of the SEM

Here, we focus only on some of the most important features of the method, and we refer the reader to Komatitsch and Vilotte (1998), Fichtner (2010), or Peter et al. (2011) for more details.

The strong form of the wave equation for viscoelastic materials is described as

$$\rho \partial_t^2 \mathbf{u} = \nabla \cdot \boldsymbol{\sigma} + \mathbf{f}, \tag{1}$$

where ρ denotes the mass density, $\mathbf{u} = \mathbf{u}(\mathbf{x}, t)$ is the displacement field, $\mathbf{x}$ is the spatial coordinates, t is the time, $\boldsymbol{\sigma}$ is the stress tensor, and $\mathbf{f}$ is the source term. The source term for viscoelastic materials can represent, for example, a point source:

$$\mathbf{f} = -\mathbf{D} \cdot \nabla \delta(\mathbf{x} - \mathbf{x}_s) S(t), \tag{2}$$

where $\mathbf{D}$ denotes the moment tensor, $\mathbf{x}_s$ is the source position, δ is the Dirac delta distribution, and $S(t)$ is the source wavelet. Under the assumption of small perturbations, the stress tensor $\boldsymbol{\sigma}$ is linearly related to the displacement field through the constitutive relationship (Hooke's law):

$$\boldsymbol{\sigma} = \mathbf{C} : \nabla \mathbf{u}, \tag{3}$$

where $\mathbf{C}$ denotes the stiffness tensor, describing the elastic properties of the material. Because the Marseille-Benchie model is made of a viscoelastic material, equation 3 has to be modified such that the stress is determined by the entire strain history:

$$\boldsymbol{\sigma}(t) = \int_{-\infty}^{t} \partial_t \mathbf{C}(t - t') : \nabla \mathbf{u}(t') dt'. \tag{4}$$

We use the technique of Liu et al. (1976) to approximate the absorption based on a set of three Zener standard linear solids. This standard approach usually assumes that the quality factor Q does not depend on the frequency. This assumption is confirmed by our laboratory measurements, which show the same Q-factor for the PVC used in the model when measured between 250 and 650 kHz (see the "Small-scale geologic model" section). In practice, the implementation of the Zener model requires fitting Q in the frequency range of interest by using a set of relaxation mechanisms (relaxation times represented by points in the frequency range and their associated weights). A linear approach can be used by setting the optimization points at given frequencies in the frequency range of interest and then optimizing the fit for the weights (Emmerich and Korn, 1987). However, this approach does not ensure the positivity of the weights and thus the decay of the total energy.

An alternative approach is introduced by Blanc et al. (2016) to ensure that the weights are always positive and their nonlinear optimization is also more accurate in terms of fitting the constant Q approximation in the frequency range of interest. The nonlinearity means that the points and the weights are optimized to obtain a better fit of Q in the frequency range of interest. We use this approach for the simulations presented in this work.

SEM uses the weak form of the equations, which can be obtained by multiplying equation 1 with an arbitrary test function $\mathbf{w}$ and then integrating by parts over the total volume of the model Ω:

$$\int_\Omega \rho \mathbf{w} \cdot \partial_t^2 \mathbf{u} d^3x = \int_{\partial\Omega} \hat{\mathbf{n}} \cdot \boldsymbol{\sigma} \cdot \mathbf{w} d^2x - \int_\Omega \nabla \mathbf{w} : \boldsymbol{\sigma} d^3x + \mathbf{M} : \nabla \mathbf{w}(\mathbf{x}_s) S(t). \tag{5}$$

Equation 5 can be reformulated as

$$\mathbf{M}\ddot{\mathbf{u}}(t) + \mathbf{K}\mathbf{u}(t) = \mathbf{f}(t), \tag{6}$$

where $\mathbf{M}$ denotes the mass matrix and $\mathbf{K}$ denotes the stiffness matrix. In SEM, the computational cost is optimized by combining high-degree Lagrange interpolants to represent the wavefield and the Gauss-Lobatto-Legendre (GLL) quadrature to compute the integrals involved (Komatitsch and Vilotte, 1998). This combination leads to a perfectly diagonal mass matrix in equation 6, which then enables the use of an explicit time scheme that can be efficiently parallelized (Komatitsch et al., 2003; Carrington et al., 2008; Vos et al., 2010). On the one hand, SEM is efficient in handling complex geometries and fluid-solid coupling. On the other hand, the standard GLL quadrature requires a hexahedral mesh in three dimensions, which can be challenging to obtain in case of a nonstructured mesh for realistic geologic setups.

Considering only a part of the full physical-domain results in the need for artificial boundaries in the simulations. To avoid spurious reflections from these boundaries, we use a perfectly matched layer (PML) technique (Komatitsch and Tromp, 2003; Festa et al., 2005; Kristek et al., 2009). Because SEM uses the weak form of the wave equation, the PML equations have singularities that need to be explicitly removed (Xie et al., 2016).

In our work, we used the Specfem3D-Cartesian, an open-source spectral-element software package (Komatitsch and Vilotte, 1998), with explicit second-order Newmark time stepping (Hughes, 1987).

Meshing

Creating a nonstructured hexahedral mesh for a complex geometry is a challenging and lengthy task (Shepherd and Johnson, 2008; Staten et al., 2010). We used Cubit/Trelis (Blacker, 1994) to mesh the model. In the case of a nonstructured mesh, we need to keep in mind the future computational cost and the accuracy by considering three points. First, the element size must be small enough to accurately model the highest frequencies to be considered. Second, the size of the different elements in one material should be as equal as possible (depending on the geometry) to avoid too-small elements. This is important because smaller elements require smaller time steps (i.e., higher computational cost) and more memory. Finally, one needs to avoid creating too-distorted/-elongated elements, which could result in a mesh of poor quality or even containing elements with negative Jacobians, making the simulation unstable. Because the model has a complex overall geometry, fully automatic hexahedral meshing algorithms could not be used. Our solution was to cut the domain into several subdomains, which were easier to handle for the meshing algorithms (Figure 3). The challenge of the task was to find the order in which the individual subdomains had to be meshed, such that the entire computational domain could be meshed at the end. Due to these difficulties, and also to reduce the computational cost, we considered only a part of the full model for the numerical simulations (Figure 3). As a result, the truncated

dome was excluded from the simulations because this object proved to be too complex to be meshed, mainly due to its small dimensions combined with sharp edges and narrow corners. With our decomposition strategy, we first obtained a mesh containing approximately 15.6 million elements, including the water layer above the PVC. Figure 6 shows a typical distribution of the element size for the model with the applied decomposition and meshing strategy. The maximum edge length is about four times bigger than the smallest one, being approximately 1.6 and 0.4 mm, respectively. It is important to note that the accuracy of the spectral-element simulations is not directly constrained by the element size, but rather by the number of GLL points per wavelength. The initial meshing strategy was designed for fourth-order polynomial basis functions, requiring five GLL points per wavelength, which is approximately five GLL points per element (Mulder, 1999). Considering the minimum velocity of the model — namely, 1050 m/s for the S-waves in PVC — and the maximum target frequency (650 kHz), the goal was to have all the edge lengths less than 1.6 mm. We present an optimized meshing strategy in Appendix A, which allowed us to reduce the number of elements to approximately 1.4 million and the computational cost by a factor of four to six.

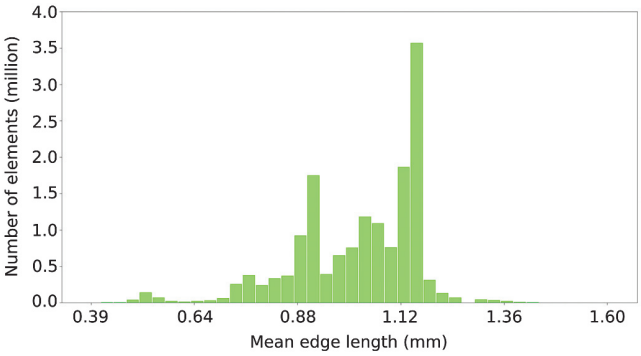

Figure 6. Distribution of the element size of the mesh for the part shown in Figure 3.

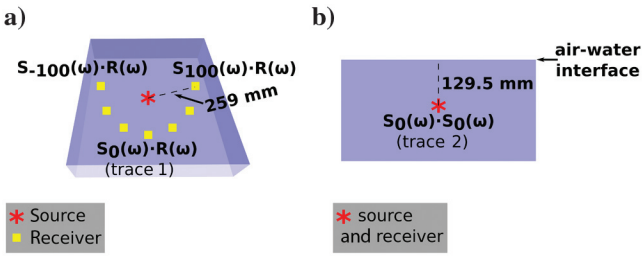

Figure 7. Schematic diagrams of laboratory characterization of (a) the source transducer using the source and receiver transducers and (b) the source transducer illuminating the air-water interface at normal incidence.

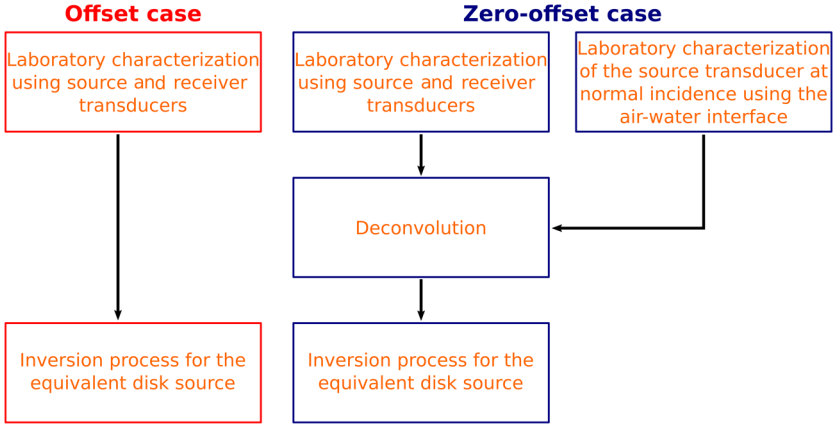

Figure 8. Workflow of the procedures used to implement the numerical equivalent of the real source transducer in offset and zero-offset configurations.

Numerical implementation of the real transducer characteristics

One of the most important tasks in our work was to accurately implement the real characteristics of the transducers in the numerical simulations. Because it is omnidirectional and has a frequency-independent sensitivity, the Teledyne Reson® hydrophone (used as the receiver for offset measurements) was implemented as a point receiver. However, the Imasonic® source transducer has a unique radiation pattern that cannot be described by the classic analytical formulation of Zemanek (1971), or by an approximate radiation pattern valid only for the dominant frequency (Tantsereva et al., 2014a). The latter does not provide a good solution because other frequencies also contribute to the radiation pattern. Therefore, we propose a new, two-step approach to implement the real transducer characteristics in numerical simulations, accounting for all frequencies. The procedure consists of laboratory characterization of the source followed by an inversion step to obtain a numerically equivalent source.

The characterization of the radiation pattern of the source transducer was performed in a water tank. The source transducer was connected to a pulse generator and kept fixed, whereas the hydrophone was moved around the source to record the impulse response of the source at every 0.2°, covering an angle range of 200° at a constant distance of 259 mm (Figure 7). The recorded data set was the input for the subsequent inversion step. Here, we need to distinguish the procedures to obtain the numerically equivalent source in zero-offset and offset configurations because they require a slightly different approach (Figure 8). We first introduce the procedure for the offset case, and the differences for the zero-offset case are discussed afterward.

Because most of the numerical tools can use point sources, we built an equivalent disk source of several point sources. This approach is based on the theory of wave superposition (Koopmann et al., 1989). The disk is described by three parameters: thickness, radius, and the number of point sources distributed on the surface. The different point sources are independent; i.e., they can have any arbitrary (smooth) source signal and are constrained only by the measured data set and the inversion process. The goal of the inversion was to determine the source signal of each point source, such that the resulting overall source signal of the whole equivalent source is the same as the one measured at each angle. The initial guess for each point source was a constant zero pressure, and the cost function was computed using the L2-norm:

$$\Phi^{(k)} = \Sigma_i \Sigma_j (m_{ij} - c_{ij})^2, \quad (7)$$

where $\Phi^{(k)}$ denotes the cost function after the kth iteration, and m_{ij} and c_{ij} are the recorded and the calculated impulse responses at the ith time sample and jth hydrophone position, respectively. During the inversion step, some parameters, namely, the radius of the equivalent disk, the number of point sources distributed on the disk, the number of layers in the disk, and the number of iterations, were tested to find the best fit with the measured data. We found that a radius of 3 mm with 253 point sources distributed on only one disk layer gives the best fit between the measured and the inverted radiation patterns (Figure 9). Using more than 10,000 iterations did not result in any significant change in the results. The comparison of simulated traces using the inverted equivalent source with the measured traces shows an angle dependency in the goodness of fit (Figure 9). Indeed, the main lobe of the radiation pattern (corresponding to $\pm 30^{\circ}$ around the center of the transducer) is accurately recovered. For example, the correlation coefficients between the measured and simulated traces at 0° and 20° are 0.99 and 0.98, respectively (Figure 10). However, outside of the range of $\pm 30^{\circ}$, the goodness of fit drastically decreases with increasing angle from the center of the transducer (Figure 9). For example, the correlation coefficient between the measured and simulated traces at 60° is 0.64 (Figure 10). Therefore, the secondary lobes of the real radiation pattern are less accurately recovered. This can be explained by the fact that the recorded signals corresponding to the secondary lobes have far less energy than those of the main lobe (less than −20 dB). Hence, they can be overshadowed by the noise recorded in the laboratory data.

The procedure to obtain the numerically equivalent source in the zero-offset configuration is quite similar to the previous one, but it requires a deconvolution process before the inversion step (Figure 8). This is due to the fact that for zero-offset measurements the same source transducer is used twice (first as the source and then as the receiver). Therefore, an extra measurement is needed, using only the source transducer to measure the reflected wavefield from the water-air interface at normal incidence (at a distance of half of 259 mm). The deconvolution process is done in the frequency domain after a Fourier transform of all the recorded signals. Let us denote the laboratory trace recorded by the hydrophone opposite to the source transducer as trace 1 (Figure 7) and the trace recorded by the source transducer corresponding to the reflected wavefield from the water-air interface at normal incidence as trace 2 (Figure 7). The process can be summarized as follows:

Step 1) Note that trace 2 is the square of the source transfer function. Therefore, the square root of trace 2 gives the source transfer function at 0°, i.e., in the opposite position to the source.

Step 2) Because the hydrophone is omnidirectional, the receiver transfer function is the same at each angle α. Therefore, divide trace 1 by the source transfer function (step 1) to determine the receiver transfer function ($R(\omega)$).

Step 3) Divide all the traces recorded by the hydrophone with the receiver transfer function (step 2) to get $S_\alpha(\omega)$ for each angle α (deconvolution in the time domain).

Step 4) Take the square of $S_\alpha(\omega)$ for each α to obtain the zero-offset transfer function of the source transducer at each angle.

Step 5) Inverse Fourier transform all the obtained traces to the time domain.

The data set derived using this deconvolution process is the input to the inversion process, which is the same as described above for the general offset case. According to our tests, the best fit between the measured and the inverted radiation patterns can be obtained with a disk radius of 6 mm, using 253 point sources and only one disk layer. Similar to the offset case, using more than 10,000 iterations did not provide better results. The angle dependency in the goodness of fit is also valid for the zero-offset case. However, the range of accurate fit is broader (approximately $\pm 35^{\circ}$ around the center of the transducer). This is due to the fact that (relatively) more energy is focused in the central beam in this configuration; thus, the outer region (with lower signal-to-noise ratio) has less influence on the inversion of the main lobe.

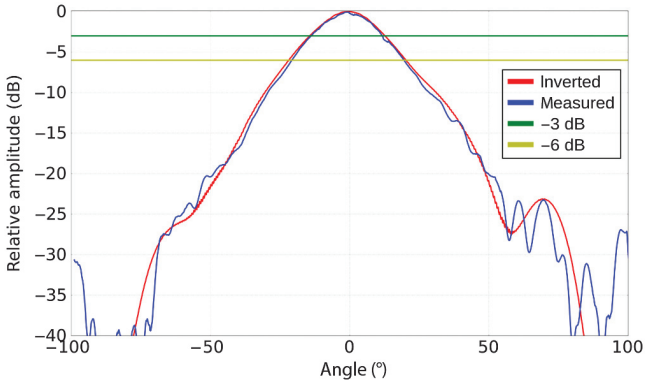

Figure 9. Comparison of the measured (blue) and inverted (red) radiation patterns of the transducer in offset configuration. The amplitude is maximal opposite to the transducer (0°).

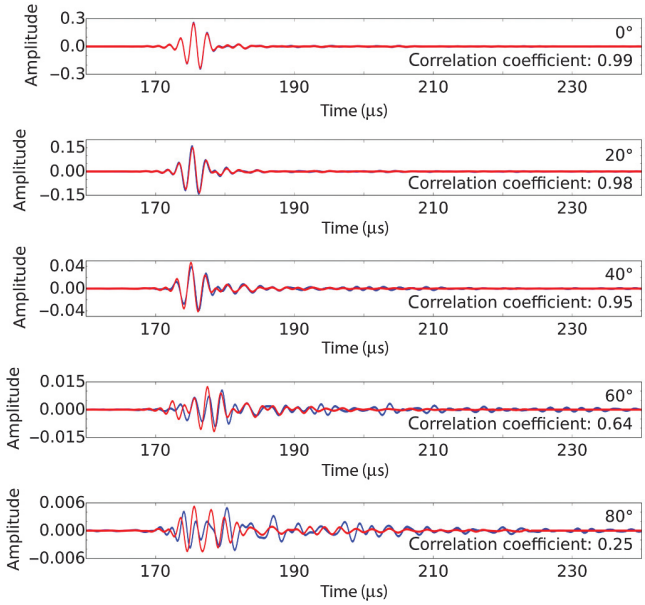

Figure 10. Comparison of the measured traces (blue) with the simulated traces (red), using the inverted equivalent source, at different angles. The correlation coefficients are shown in each panel, respectively.

Numerical calibration of material properties

Because the characterization of material samples yields a range of values for each measured property, an initial calibration was necessary to find the values to be used for the final simulations. To have the least geometric effect on the calibration, a test point above the flat part of the model was chosen (the black cross in Figure 11), far from the sides of the model to avoid edge effects as much as possible. For this point, the laboratory trace was considered to be the reference, and the following properties were tested during the calibration simulations: velocity and Q-factors for P- and S-waves for the PVC. The densities of PVC and water and the velocity of P-waves in water were considered to be known.

We note here that the investigated parameters have a combined effect on the amplitude, phase, and arrival times, so the result of this calibration provides one possible solution in the parameter space. First, the velocities of P- and S-waves for the PVC were calibrated, then all the remaining differences between the reference laboratory trace and the simulated trace were attributed to Q_P and Q_S.

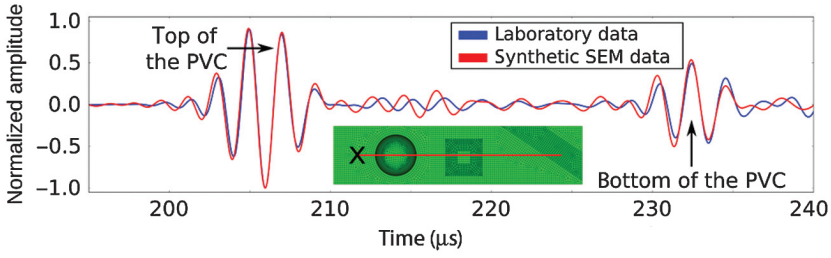

Figure 11. Comparison of zero-offset laboratory trace with synthetic results for the test point to calibrate the material properties before the final simulations. The position of the test point is shown with the black cross.

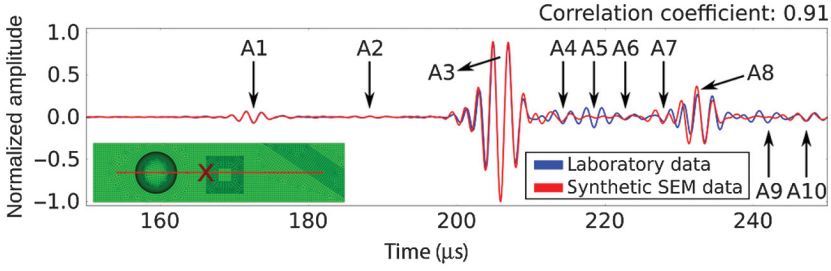

Figure 12. Comparison of zero-offset laboratory trace A with synthetic results. Physical interpretation of the annotated events is provided in the text.

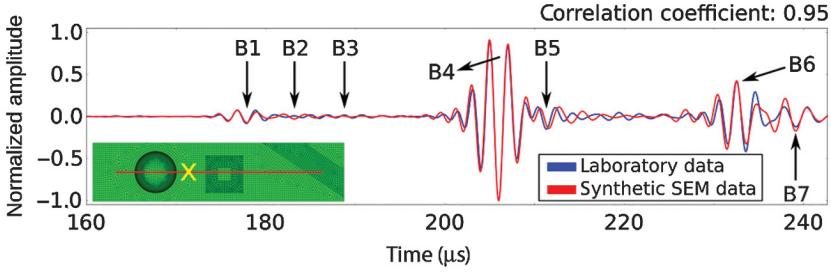

Figure 13. Comparison of zero-offset laboratory trace B with synthetic results. Physical interpretation of the annotated events is provided in the text.

The resulting material parameters from the calibration are as follows: $V_P = 2260$ m/s, $V_S = 1050$ m/s, $\rho = 1412$ kg/m^3, $Q_P = 28.7$, and $Q_S = 26$.

DATA COMPARISONS

Comparison of zero-offset data

Here, we consider more specifically three traces of the laboratory zero-offset section, shown in Figure 4 and corresponding to the red line in Figure 3. These traces (labeled as A, B, and C in Figure 4) are of particular interest because they contain diffracted waves generated by the feature edges, as well as reflections from the flat and curved surfaces of the model.

Trace A is located above the lower edge of the pyramid, in which its flank meets the flat part (Figure 12). It is composed of several groups of reflections from the side of the pyramid (denoted as event A1), from the flat part (A3 and A4), from the bottom of the model below the flat part (A8 and A9), and below the dome (A10). Several groups of diffracted waves are also present, corresponding to diffractions from the upper edge (A2) and the lower edge (A7) of the pyramid, and from the edge of the dome (A6). Event A5 is related to the truncated dome, which is not included in the simulations.

Trace B is located half-way between the pyramid and the dome (Figure 13). It is composed of several groups of events associated with reflections from the side of the dome (events B1 and B2), from the side of the pyramid (B3), from the flat part (B4), and from the bottom of the model below the flat part (B6). Event B5 is the superposition of diffractions from the upper edge of the pyramid and from the edge of the dome. Event B7 corresponds to the superposition of a reflection from the bottom of the model below the dome and a diffraction from the lower edge of the pyramid.

Trace C is located on the other side of the dome, compared with traces A and B (Figure 14). It is composed of several groups of reflections from the side of the dome (C1 and C2), from the flat part (C3 and C4), and from the bottom of the model below the flat part (C6 and C7). Event C5 is a multiple of a diffraction from the lower edge of the dome, whereas event C8 is a multiple reflection.

It is important to note that the laboratory data are real data because they contain unknown noise recorded by the acquisition system. Furthermore, as shown in Figure 2, the source wavelet is a long signal, composed of a main event followed by a few tens of μs long low-energy tail with small amplitudes (ringing effect). It may explain the fact that some events are composed of two parts (e.g., events A8 and A9 in Figure 12; B1 and B2 in Figure 13; C1 and C2, C3 and C4, C6 and C7 in Figure 14).

Qualitative comparisons between laboratory and synthetic traces show a quite good fit in am-

plitude, phase, and traveltime. Regardless of the trace location, synthetic traces show an almost perfect fit with the experimental data in time, phase, and amplitude for the reflected events from the top and bottom of the flat part of the model. The early and late parts of these arrivals sometimes reveal minor amplitude misfits, most probably due to the low-energy second part of the source signal, which may not be perfectly reconstructed by the source inversion, as well as the uncertainties in the attenuation parameters chosen for the simulations. Events associated with the side reflections and/or diffractions from the topographic features are also well restored by the simulations (see events A1 in Figure 12, B5 and B6 in Figure 13, and C1 and C8 in Figure 14). The correlation coefficients between the measured and simulated traces are 0.91, 0.95, and 0.91 for traces A, B, and C, respectively. These good results are due to the fact that SEM has the ability to honor the model geometry, even for tilted and curved interfaces by using a nonstructured mesh.

Comparison of offset data

Here, we consider more specifically one trace of the laboratory offset section, labeled D in Figure 5. The source location (represented by the asterisk in Figure 15) is above the flank of the dome, and the receiver (represented by the triangle in Figure 15) is located close to the ramp. Trace D contains several groups of events, mainly associated with the direct source-receiver travel path (labeled as D1 in Figure 15), the reflection from the top of the truncated pyramid (D2), and the reflection from the curved surface of the dome (D3).

A qualitative comparison between the simulated results and laboratory data shows a good fit in arrival time, phase, and amplitude for all the events pointed out, except for the reflection from the dome (D3). Some important remarks must be highlighted here. First, the offset configurations are more sensitive to noise than the zero-offset ones. Due to a more complex acquisition setup, using more electric devices and transducers, the signal-to-noise ratio of the laboratory data in the offset configuration is generally lower than in the zero-offset case. Furthermore, the offset configurations are also more sensitive to uncertainties in the acquisition geometry, especially in the case of a model with strongly tilted and curved interfaces. Indeed, it can be analytically shown that a small uncertainty in the source position and/or in the incidence angle of the incident wave may have a significant impact on the illumination of the curved surface of the dome. As a result, it can have a huge effect on the reflected and diffracted wavefields (see the "Discussion" section). It explains the fact that event D3 in Figure 15 is quite well-modeled by the simulation, but with significant time and amplitude misfits. The correlation coefficient between the measured and simulated traces is 0.76 for trace D. Finally, as mentioned above, the implementation of the numerically equivalent source has higher uncertainties for the low-energy later part of the source wavelet and the secondary lobes (due to the low signal-to-noise ratio of these events) than for the main lobe of the directivity pattern. Even if they carry less energy than the main lobe, the role of these higher order lobes in the illumination of the model should not be neglected in the case of offset configurations.

DISCUSSION

As shown above, SEM can reproduce laboratory zero-offset data in terms of arrival time, phase, and amplitude with excellent accuracy. However, the fit between synthetic results and experimental offset data is significantly less accurate. We discuss here the possible explanations for this observation, including experimental uncertainties and numerical implementation of the directivity pattern of the source transducer, as well as the computational cost.

Laboratory data always contain noise, and offset data sets have a lower signal-to-noise ratio than zero-offset ones. Moreover, uncertainties in the transducer positions also have an effect on the data. It is more significant in the offset case because there is a nonlinear combination of uncertainties in the source location, the source tilt angle, and the receiver position. This nonlinear combination makes it difficult to evaluate the role of one effect over the others. This effect is even more pronounced in the presence of strongly curved interfaces, causing wave defocusing. Let us analyze here this source of misfit and quantify the order of magnitude of the possible resulting error. Because the problem is the most pronounced in the case of strongly curved interfaces, we show an example for the Marseille-Benchie model using the dome.

The geometry of the problem is shown in Figure 16, and for now we suppose that the source is located exactly above the top of the dome. We are interested in the change in the offset of the arrival of a given ray due to an error in the tilt angle of the source (γ). Based on geometric considerations, we can obtain the following relations:

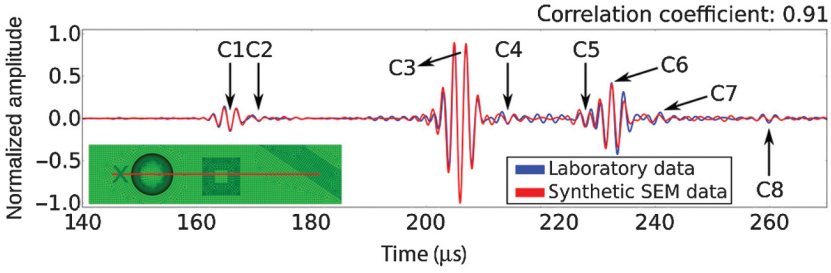

Figure 14. Comparison of zero-offset laboratory trace C with synthetic results. Physical interpretation of the annotated events is provided in the text.

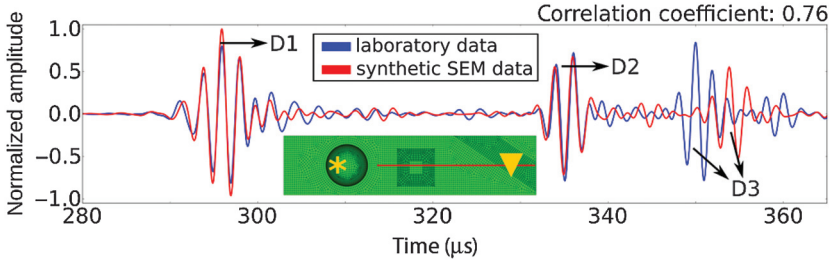

Figure 15. Comparison of offset laboratory trace D with synthetic results. Physical interpretation of the annotated events is provided in the text. The red line shows the acquisition line, the yellow asterisk shows the source position, and the yellow triangle shows the receiver corresponding to trace D.

$$\delta x = \frac{R+H}{\cos^2(\Theta)}\delta\Theta \tag{8}$$

and

$$\delta y = \delta l_2 \frac{\sin(\alpha)}{\cos(\Theta+\alpha)} + l_2 \frac{\cos(\alpha)\delta\alpha\cos(\Theta+\alpha)+\sin(\Theta+\alpha)(\delta\Theta+\delta\alpha)\sin(\alpha)}{\cos^2(\Theta+\alpha)}, \tag{9}$$

where the offset change is the sum of δx and δy, R denotes the radius of the dome, and H is the distance between the top of the dome and the source transducer. To quantify the order of magnitude of the error in the offset, we consider $H = 140$ mm, $R = 51.25$ mm, and $\gamma = 5^\circ$. Supposing an error of 0.5° in the source position, the point of illumination on the surface of the dome has an error of 1.3 mm. Using equations 8 and 9 above, we get $\delta x = 5.2$ mm and $\delta y = 1.5$ mm. This means that an uncertainty of 0.5° in the source tilt angle leads to a shift of 6.7 mm (134 m at seismic scale) in the arrival offset of the beam (i.e., in the receiver location), depending on the point of the illumination of the surface of the dome. This uncertainty may thus have a significant impact on the arrival time and the amplitude of the reflected and diffracted events. In ongoing work, we now focus on the design of an acquisition system providing much higher accuracy of transducer positions to significantly decrease these uncertainties in the recorded data.

We have proposed a strategy to numerically implement the directivity pattern of the real source transducer. This strategy permits to recover the main lobe of the emitted beam, in which most of the energy is concentrated. The excellent fit between synthetic results and laboratory zero-offset data shows that the strategy is efficient in zero-offset configurations because the main lobe mostly illuminates the model and contributes to the recorded data. Nevertheless, for offset data recorded in strong topographic environments, the proposed strategy is less accurate because the low-energy later part of the source wavelet (see Figure 2) and the secondary lobes play an important role in the illumination of the model, even if they carry far less energy than the main event of the source wavelet in the main lobe. Indeed, in our case, they may interact with the dome and the pyramid (depending on the source location), influencing the amplitude and phase of the wavefield. Future work will focus on a new approach to numerically implement real transducer properties, which can accurately account for the main lobe and the lower energy parts of the source wavelet.

The computational cost of numerical methods is often an important point, particularly in the operational context of seismic exploration. Here, we differentiate between the man-hour cost spent on the preparation of the simulations and the computational cost (i.e., the number of processors used for simulations times the actual running time of one simulation). In general, SEM has a large man-hour cost, due to the nonstructured hexahedral meshing. To illustrate this problem, we note that we spent three weeks to find the optimal meshing strategy for the Marseille-Benchie model, without finding a satisfying strategy for the truncated dome. Contrary to the common finite-difference gridding, there is no quick or cheap solution to nonstructured hexahedral meshing in terms of man-hour cost.

Regarding the computational cost of the method, we used 2100 Intel Xeon Sandy Bridge EP (E5-2680) processor cores for the simulations. The initial meshing strategy resulted in a mesh that needed 10,150 core hours to simulate 350 μs of wave propagation (corresponding to 7 s at seismic scale). Using the optimized meshing strategy of Appendix A, this cost was reduced to 1611 core hours with a relative element size of 2.5, or to 2538 core hours with a relative element size of 2.25.

CONCLUSIONS AND FUTURE WORK

The goal of our work is to provide a possible workflow to adapt the numerical simulations and the small-scale laboratory experiments to each other, such that the two can be easily compared with high accuracy. We are also interested in the ability of SEM to accurately simulate complex 3D wavefields including (multiple) diffractions at the lowest possible computational and man-hour cost. We have thus compared 3D SEM simulations with laboratory measurements in 3D zero-offset and 3D offset offshore reflection configurations for a small-scale physical model. The model includes structures with steep flanks, sharp edges, corners, and curved interfaces. This complexity provides a challenge to any numerical method to reproduce the wavefield.

Prior to the simulations, some works have focused on the input data/parameters, such as the material properties, the model geometry, and the characteristics of the source and receiver transducers. The viscoelastic behavior of the material used in the model has been approximated with a set of Zener standard linear solids, whereas the other parameters are known from previous laboratory characterization of material samples. The real source transducer characteristics have been implemented based on a new approach: laboratory characterization of the impulse response, followed by an inversion step to obtain a numerically equivalent source for the numerical simulations. The zero-offset measurement requires an additional deconvolution step before the inversion because, in that case, only one transducer is used as the source and the receiver.

We have suggested an optimization of the computational cost, by using larger elements in the nonstructured mesh and higher order polynomial basis functions. This technique helps to

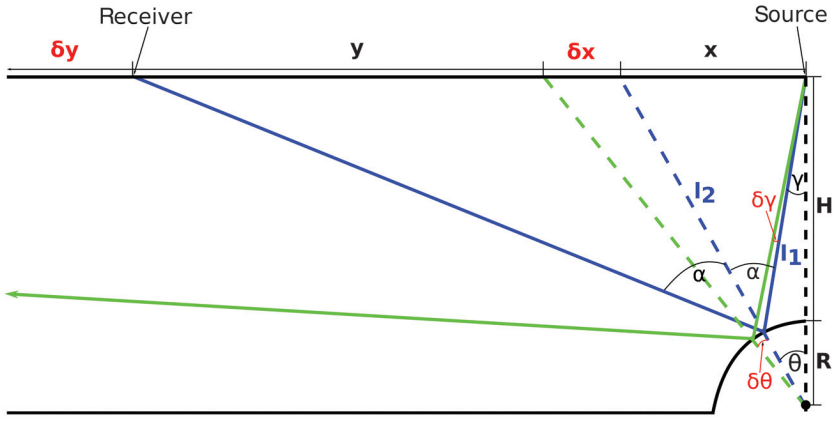

Figure 16. The effect of the uncertainties in the source position on the wavefield.

significantly reduce the computational cost, while obtaining a similar level of accuracy.

Comparison of the zero-offset synthetic and laboratory results has revealed an excellent fit in terms of arrival time, phase, and amplitude. Minor amplitude mismatches may be attributed to the noise recorded in the laboratory data, as well as to the inaccuracy of the proposed source implementation to restore the low-energy secondary lobes of the source transducer, and the uncertainties in the attenuation parameters chosen for the simulations. Comparison of simulated and laboratory offset traces has exhibited a good fit in terms of amplitude, arrival time, and phase, but with significantly less accuracy for some arrivals than in the zero-offset case. This can be mainly attributed to the inaccuracies of the transducer positions during the laboratory measurements combined with the strong topography of the model, as well as to the smaller signal-to-noise ratio of the offset configurations.

Future work will focus on the development of a more accurate acquisition system to reduce inaccuracies in transducer positions during the laboratory measurements. Furthermore, the noise level of the new acquisition system will have to be assessed. The proposed numerical implementation of the real transducer should also be investigated further, to account more for the low-energy secondary lobes, and the low-energy later arrivals of the source signal as well, because they may also contribute to the wavefield. The reduction of the man-hour cost of SEM, due to the lengthy meshing step, will be essential in the future. A more robust and automatic meshing tool, suitable for nonstructured hexahedral meshing of arbitrary 3D geometries will be required. The laboratory data sets and the obtained numerical results should also be compared with other numerical methods, such as the commonly used finite-difference method.

ACKNOWLEDGMENTS

The authors thank Z. Xie for his help with the implementation of stable PMLs for the 3D case, E. Casarotti for his advices on nonstructured meshing, and R. Guillermin, P. Sanchez, G. Rabau, and V. Long for their help with the experiments. This work received funding from the European Union Horizon 2020 research and innovation program under the Marie Sklodowska-Curie grant, agreement no. 641943. B. Arntsen and B. Ursin received financial support from the Norwegian Research Council through the ROSE project. We also thank CNRS for its financial support through the PICS BENCHIE project. This work was granted access to the French HPC resources of TGCC under allocations no. 2016-gen7165 and 2017-gen7165 made by GENCI. We also acknowledge the associate editor and the anonymous reviewers for their careful reading, helpful suggestions, and questions, which all improved the paper.

APPENDIX A

MESH OPTIMIZATION TO REDUCE THE COMPUTATIONAL COST

As mentioned in the "Meshing" section, finding the appropriate meshing strategy for a complex geometry using a nonstructured hexahedral mesh is a time-consuming procedure. Thus, our goal here is to reduce the computational cost without modifying the meshing strategy. In other words, we use the same subdivision of the whole model into subdomains and the same meshing order of the different subdomains.

Our optimization takes advantage of the fact that the accuracy of the spectral-element simulations is not directly constrained by the element size, but rather by the number of GLL points per wavelength. This means that we can increase the element size and keep a similar level of accuracy of the simulations by increasing the order of the polynomial basis functions. This technique is widely discussed in the literature as $h-$, $p-$, or $h-p$ convergence, where h stands for the element size and p denotes the polynomial order of the basis functions (e.g., Hughes, 1987; Maday and Rønquist, 1990; Seriani and Priolo, 1994; Vos et al., 2010; Oliveira and Seriani, 2011). For the initial meshing of the model, we used basis functions of order $N = 4$, meaning that $N + 1 = 5$ GLL points are used in each element.

We consider the mesh presented in Figure 3 as the reference for this Appendix. As shown in the "Comparison of zero-offset data" section, the reference mesh yields accurate synthetic results compared with the zero-offset laboratory data. When creating a nonstructured mesh, the element size has a distribution as shown in Figure 6. This is due to the geometric constraints on the meshing algorithm, resulting in various element sizes. Cubit/Trelis uses a target element size because the meshing algorithm aims to mesh the model such that the average of the element sizes is close to this target value. For the reference mesh, a target edge length of 1.1 mm is necessary to have the largest elements below the required threshold of 1.6 mm. For the sake of brevity, we use relative target element sizes hereafter, by considering the target element size of the reference mesh as being equal to one. We note that small changes in the target element size result in the same distribution of the element sizes; only the size of each element is multiplied by the factor of the change. According to our experience, this remains true even for such a complex geometry as the Marseille-Benchie model if the change is at most a factor of 0.2–5. Because our meshing strategy involves the subdivision of the model into several subdomains, there is an upper limit for increasing the element size. With our decomposition strategy, using approximately five times larger elements than the reference value is the upper limit. It comes from the fact that above this value, the element size becomes too high compared with the dimensions of some of the subdomains. We emphasize that using larger elements does not result in a less accurate representation of even the curved interfaces because curved hexahedral elements are used. It means that the numerical tool can account for curved edges and surfaces of each element, instead of only straight lines and planar surfaces (Komatitsch and Vilotte, 1998; Fichtner, 2010).

We tested two different approaches. The first one consists of fixing the polynomial order of the basis functions and changing the element size. The second one keeps the element size fixed and changes the polynomial order. To evaluate the results, we ran the same zero-offset simulations using the different meshes and compared the resulting synthetic traces with traces obtained with the reference mesh. To evaluate the tests, we use zero-offset traces B and C (Figures 13 and 14). To obtain a quantitative comparison, we computed the root-mean-square (rms) difference between each synthetic trace and the reference trace. Figure A-1 shows the relative computational cost and the rms misfit for different element sizes, using the sixth-order polynomial basis functions. The results suggest that the optimum is around relative element sizes of 2.25–2.5.

Using smaller elements increases the computational cost, whereas using larger elements increases the rms misfit without any significant gain in the relative computational cost.

Considering that the optimal element size is approximately 2.5 (based on Figure A-1), the effect of the polynomial order has to be examined as well. Figure A-2 shows the relative computational cost and the rms misfit for different polynomial orders, using a relative element size of 2.5. The results show that the polynomial order of eight yields the smallest rms misfit (approximately 0.008). Even though the rms misfit is somewhat higher for order six (approximately 0.05), its computational cost is more than three times lower than that of order eight. We note that the rms misfit does not show a monotonous trend for any of the traces, neither in Figure A-1 nor in Figure A-2. This is probably due to the nonstructured mesh. Maday and Rønquist (1990) mathematically prove that a monotonous trend in the misfit curves can be expected only for a structured mesh, but not necessarily for a nonstructured mesh.

Figure A-3 shows the comparison of the traces using the optimized mesh (relative element size of 2.5) and sixth-order basis functions with the reference traces. The optimized mesh provides an excellent fit with the reference solutions in general. Due to the larger elements, some minor oscillations can be seen, probably due to mesh dispersion. However, their amplitude and difference from the reference solutions are negligible. Considering that the relative computational cost is only 15.7% of the reference simulation, we suggest to use the optimized meshing strategy. Moreover, the effect of mesh dispersion can be reduced by using a relative element size of 2.25 instead of 2.5. In that case, the relative computational cost is still 25% of the reference, in return for a bit higher accuracy than with a relative element size of 2.5.

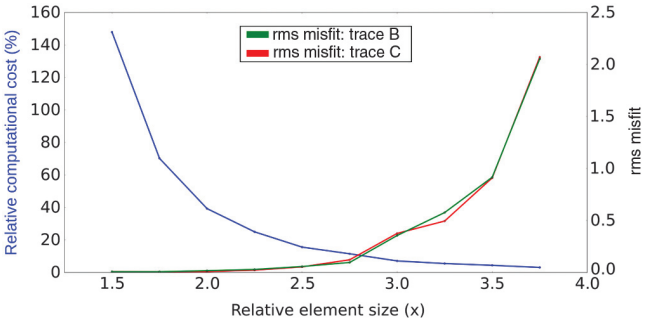

Figure A-1. Relative computational cost (blue) and rms misfit (green: trace B, red: trace C) for varying element size, using the sixth-order polynomial basis functions.

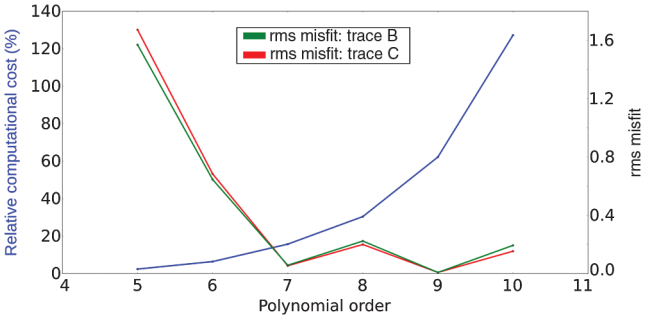

Figure A-2. Relative computational cost (blue) and rms misfit (green: trace B, red: trace C) for varying order of the polynomial basis functions, using a relative element size of 2.5.

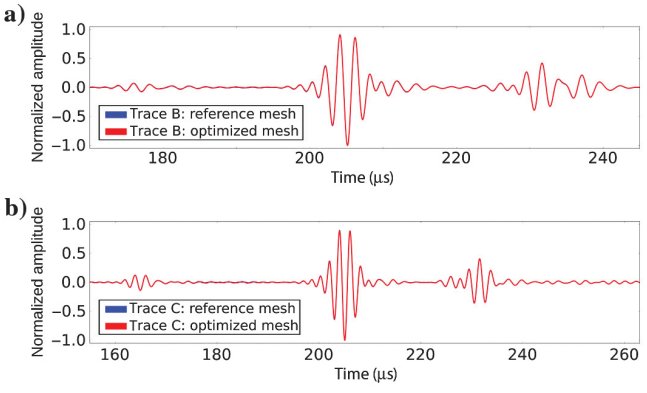

Figure A-3. Comparison of zero-offset synthetic traces using the reference mesh (blue) and the optimized mesh with a relative element size of 2.5 and sixth-order basis functions (red): (a) trace B and (b) trace C.

REFERENCES

Blacker, T., 1994, Cubit mesh generation environment users manual, https://cubit.sandia.gov/public/13.2/help_manual/WebHelp/cubit_users_manual.html, accessed 15 February 2018.

Blanc, E., D. Komatitsch, E. Chaljub, B. Lombard, and Z. Xie, 2016, Highly-accurate stability-preserving optimization of the Zener viscoelastic model, with application to wave propagation in the presence of strong attenuation: Geophysical Journal International, **205**, 414–426, doi: 10.1093/gji/ggw024.

Bretaudeau, F., R. Brossier, D. Leparoux, O. Abraham, and J. Virieux, 2013, 2D elastic full-waveform imaging of the near-surface: Application to synthetic and physical modelling data sets: Near Surface Geophysics, **11**, 307–316, doi: 10.3997/1873-0604.2012067.

Bretaudeau, F., D. Leparoux, O. Durand, and O. Abraham, 2011, Small-scale modeling of onshore seismic experiment: A tool to validate numerical modeling and seismic imaging methods: Geophysics, **76**, no. 5, T101–T112, doi: 10.1190/geo2010-0339.1.

Campman, X. H., K. van Wijk, J. A. Scales, and G. C. Herman, 2005, Imaging and suppressing near-receiver scattered surface waves: Geophysics, **70**, no. 2, V21–V29, doi: 10.1190/1.1884831.

Capdeville, Y., E. Chaljub, and J. Montagner, 2003, Coupling the spectral element method with a modal solution for elastic wave propagation in global earth models: Geophysical Journal International, **152**, 34–67, doi: 10.1046/j.1365-246X.2003.01808.x.

Capdeville, Y., C. Larmat, J.-P. Vilotte, and J.-P. Montagner, 2002, A new coupled spectral element and modal solution method for global seismology: A first application to the scattering induced by a plume-like anomaly: Geophysical Research Letters, **29**, 32-1–32-4.

Carrington, L., D. Komatitsch, M. Laurenzano, M. Tikir, D. Michéa, N. Le Goff, A. Snavely, and J. Tromp, 2008, High-frequency simulations of global seismic wave propagation using SPECFEM3D GLOBE on 62 thousand processor cores: Proceedings of the 2008 ACM/IEEE Conference on Supercomputing, 1–11 (Article #60, Gordon Bell Prize finalist article).

Chai, X., S. Wang, J. Wei, J. Li, and H. Yin, 2015, Reflectivity inversion for attenuated seismic data: Physical modeling and field data experiments: Geophysics, **81**, no. 1, T11–T24, doi: 10.1190/geo2015-0250.1.

Chaljub, E., E. Maufroy, P. Moczo, J. Kristek, F. Hollender, P.-Y. Bard, E. Priolo, P. Klin, F. De Martin, and Z. Zhang, 2015, 3D numerical simulations of earthquake ground motion in sedimentary basins: Testing accuracy through stringent models: Geophysical Journal International, **201**, 90–111, doi: 10.1093/gji/ggu472.

Chang, C.-H., Y.-F. Chang, and P.-Y. Tseng, 2017, Azimuthal variation of converted-wave amplitude in a reservoir with vertically aligned fractures — A physical model study: Geophysical Prospecting, **65**, 221–228, doi: 10.1111/1365-2478.12357.

Cooper, J. K., D. C. Lawton, and G. F. Margrave, 2010, The wedge model revisited: A physical modeling experiment: Geophysics, **75**, no. 2, T15–T21, doi: 10.1190/1.3309641.

De Basabe, J. D., and M. K. Sen, 2014, A comparison of finite-difference and spectral-element methods for elastic wave propagation in media with

a fluid-solid interface: Geophysical Journal International, **200**, 278–298, doi: 10.1093/gji/ggu389.
Ebrom, D. A., and J. A. McDonald, 1994, Seismic physical modeling: SEG.
Ekanem, A., J. Wei, X.-Y. Li, M. Chapman, and I. Main, 2013, P-wave attenuation anisotropy in fractured media: A seismic physical modelling study: Geophysical Prospecting, **61**, 420–433, doi: 10.1111/j.1365-2478.2012.01127.x.
Emmerich, H., and M. Korn, 1987, Incorporation of attenuation into time-domain computations of seismic wave fields: Geophysics, **52**, 1252–1264, doi: 10.1190/1.1442386.
Favretto-Anrès, N., and G. Rabau, 1997, Excitation of the Stoneley-Scholte wave at the boundary between an ideal fluid and a viscoelastic solid: Journal of Sound and Vibration, **203**, 193–208, doi: 10.1006/jsvi.1996.0884.
Favretto-Anrès, N., and J.-P. Sessarego, 1999, Identification of shear wave parameters of viscoelastic solids by laboratory measurements of Stoneley-Scholte waves: Acta Acustica United with Acustica, **85**, 505–516.
Favretto-Cristini, N., A. M. Aizenberg, B. Ursin, P. Cristini, and A. Tantsereva, 2017, Analysis of wave scattering from a viscoelastic layer with complex shape: Journal of Computational Acoustics, **25**, 1750023, doi: 10.1142/S0218396X17500230.
Favretto-Cristini, N., A. Tantsereva, P. Cristini, B. Ursin, D. Komatitsch, and A. Aizenberg, 2014, Numerical modeling of zero-offset laboratory data in a strong topographic environment: Results for a spectral-element method and a discretized Kirchhoff integral method: Earthquake Science, **27**, 391–399, doi: 10.1007/s11589-014-0061-4.
Fehler, M. C., and P. J. Keliher, 2011, SEAM phase I: Challenges of subsalt imaging in tertiary basins, with emphasis on deepwater Gulf of Mexico: SEG.
Festa, G., E. Delavaud, and J.-P. Vilotte, 2005, Interaction between surface waves and absorbing boundaries for wave propagation in geological basins: 2D numerical simulations: Geophysical Research Letters, **32**, doi: 10.1029/2005GL024091.
Fichtner, A., 2010, Full seismic waveform modelling and inversion: Springer-Verlag.
French, W. S., 1974, Two-dimensional and three-dimensional migration of model-experiment reflection profiles: Geophysics, **39**, 265–277, doi: 10.1190/1.1440426.
Hughes, T. J., 1987, The finite element method: Linear static and dynamic finite element analysis: Prentice-Hall International Inc.
Igel, H., N. Takeuchi, R. J. Geller, C. Megnin, H.-P. Bunge, E. Clevede, J. Dalkolmo, and B. Romanowicz, 2000, The cosy project: Verification of global seismic modeling algorithms: Physics of the Earth and Planetary Interiors, **119**, 3–23, doi: 10.1016/S0031-9201(99)00150-8.
Komatitsch, D., and J. Tromp, 2002, Spectral-element simulations of global seismic wave propagation — I. Validation: Geophysical Journal International, **149**, 390–412, doi: 10.1046/j.1365-246X.2002.01653.x.
Komatitsch, D., and J. Tromp, 2003, A perfectly matched layer absorbing boundary condition for the second-order seismic wave equation: Geophysical Journal International, **154**, 146–153, doi: 10.1046/j.1365-246X.2003.01950.x.
Komatitsch, D., S. Tsuboi, C. Ji, and J. Tromp, 2003, A 14.6 billion degrees of freedom, 5 teraflops, 2.5 terabyte earthquake simulation on the earth simulator: Proceedings of the 2003 ACM/IEEE Conference on Supercomputing, doi: 10.1145/1048935.1050155.
Komatitsch, D., and J.-P. Vilotte, 1998, The spectral element method: An efficient tool to simulate the seismic response of 2D and 3D geological structures: Bulletin of the Seismological Society of America, **88**, 368–392.
Koopmann, G. H., L. Song, and J. B. Fahnline, 1989, A method for computing acoustic fields based on the principle of wave superposition: The Journal of the Acoustical Society of America, **86**, 2433–2438, doi: 10.1121/1.398450.
Kristek, J., P. Moczo, and M. Galis, 2009, A brief summary of some PML formulations and discretizations for the velocity-stress equation of seismic motion: Studia Geophysica et Geodaetica, **53**, 459–474, doi: 10.1007/s11200-009-0034-6.
Liu, H.-P., D. L. Anderson, and H. Kanamori, 1976, Velocity dispersion due to anelasticity; implications for seismology and mantle composition: Geophysical Journal International, **47**, 41–58, doi: 10.1111/j.1365-246X.1976.tb01261.x.
Maday, Y., and E. M. Rønquist, 1990, Optimal error analysis of spectral methods with emphasis on non-constant coefficients and deformed geometries: Computer Methods in Applied Mechanics and Engineering, **80**, 91–115, doi: 10.1016/0045-7825(90)90016-F.
Mittet, R., 2017, On the internal interfaces in finite-difference schemes: Geophysics, **82**, no. 4, T159–T182, doi: 10.1190/geo2016-0477.1.
Moczo, P., J. Ampuero, J. Kristek, S. Day, M. Kristekova, P. Pazak, M. Galis, and H. Igel, eds., 2006, Comparison of numerical methods for seismic wave propagation and source dynamics — the SPICE code validation: Proceedings of International Symposium on the Effects of Surface Geology on Seismic Motion, 3, 1–10.
Moczo, P., J. Kristek, M. Galis, and P. Pazak, 2010, On accuracy of the finite-difference and finite-element schemes with respect to p-wave to s-wave speed ratio: Geophysical Journal International, **182**, 493–510.
Mulder, W., 1999, Spurious modes in finite-element discretizations of the wave equation may not be all that bad: Applied Numerical Mathematics, **30**, 425–445, doi: 10.1016/S0168-9274(98)00078-6.
Oliveira, S., and G. Seriani, 2011, Effect of element distortion on the numerical dispersion of spectral element methods: Communications in Computational Physics, **9**, 937–958, doi: 10.4208/cicp.071109.080710a.
Pageot, D., D. Leparoux, M. Le Feuvre, O. Durand, P. Côte, and Y. Capdeville, 2017, Improving the seismic small-scale modelling by comparison with numerical methods: Geophysical Journal International, **211**, 637–649, doi: 10.1093/gji/ggx309.
Pant, D., S. Greenhalgh, and B. Zhou, 1992, Physical and numerical model study of diffraction effects on seismic profiles over simple structures: Geophysical Journal International, **108**, 906–916, doi: 10.1111/j.1365-246X.1992.tb03479.x.
Peter, D., D. Komatitsch, Y. Luo, R. Martin, N. Le Goff, E. Casarotti, P. Le Loher, F. Magnoni, Q. Liu, C. Blitz, T. Nissen-Meyer, P. Basini, and J. Tromp, 2011, Forward and adjoint simulations of seismic wave propagation on fully unstructured hexahedral meshes: Geophysical Journal International, **186**, 721–739, doi: 10.1111/j.1365-246X.2011.05044.x.
Pratt, R. G., 1999, Seismic waveform inversion in the frequency domain. Part I: Theory and verification in a physical scale model: Geophysics, **64**, 888–901, doi: 10.1190/1.1444597.
Robertsson, J. O., B. Bednar, J. Blanch, C. Kostov, and D.-J. van Manen, 2007, Introduction to the supplement on seismic modeling with applications to acquisition, processing, and interpretation: Geophysics, **72**, no. 5, SM1–SM4, doi: 10.1190/1.2755959.
Seriani, G., and E. Priolo, 1994, Spectral element method for acoustic wave simulation in heterogeneous media: Finite Elements in Analysis and Design, **16**, 337–348, doi: 10.1016/0168-874X(94)90076-0.
Shepherd, J. F., and C. R. Johnson, 2008, Hexahedral mesh generation constraints: Engineering with Computers, **24**, 195–213, doi: 10.1007/s00366-008-0091-4.
Sherlock, D., J. McKenna, and B. Evans, 2000, Time-lapse 3D seismic physical modelling: Exploration Geophysics, **31**, 310–314, doi: 10.1071/EG00310.
Staten, M. L., R. A. Kerr, S. J. Owen, T. D. Blacker, M. Stupazzini, and K. Shimada, 2010, Unconstrained plastering — Hexahedral mesh generation via advancing-front geometry decomposition: International Journal for Numerical Methods in Engineering, **81**, 135–171.
Stewart, R. R., N. Dyaur, B. Omoboya, J. De Figueiredo, M. Willis, and S. Sil, 2012, Physical modeling of anisotropic domains: Ultrasonic imaging of laser-etched fractures in glass: Geophysics, **78**, no. 1, D11–D19, doi: 10.1190/geo2012-0075.1.
Tantsereva, A., B. Ursin, N. Favretto-Cristini, P. Cristini, and A. M. Aizenberg, 2014a, Numerical modeling of 3D zero-offset laboratory data by a discretized kirchhoff integral method: Geophysics, **79**, no. 2, T77–T90, doi: 10.1190/geo2013-0034.1.
Tantsereva, A., B. Ursin, N. Favretto-Cristini, P. Cristini, and A. M. Aizenberg, 2014b, To: "numerical modeling of 3D zero-offset laboratory data by a discretized kirchhoff integral method": Geophysics, **79**, no. 2, Y3–Y4, doi: 10.1190/2014-0812-ERRATUM.1.
Virieux, J., H. Calandra, and R.-É. Plessix, 2011, A review of the spectral, pseudo-spectral, finite-difference and finite-element modelling techniques for geophysical imaging: Geophysical Prospecting, **59**, 794–813, doi: 10.1111/j.1365-2478.2011.00967.x.
Vos, P. E., S. J. Sherwin, and R. M. Kirby, 2010, From h to p efficiently: Implementing finite and spectral/hp element methods to achieve optimal performance for low-and high-order discretisations: Journal of Computational Physics, **229**, 5161–5181, doi: 10.1016/j.jcp.2010.03.031.
Wapenaar, C., and A. Berkhout, 1987, Three-dimensional target-oriented pre-stack migration: First Break, **5**, 217–227, doi: 10.3997/1365-2397.1987011.
Xie, Z., R. Matzen, P. Cristini, D. Komatitsch, and R. Martin, 2016, A perfectly matched layer for fluid-solid problems: Application to ocean-acoustics simulations with solid ocean bottoms: The Journal of the Acoustical Society of America, **140**, 165–175, doi: 10.1121/1.4954736.
Xu, C., B. Di, and J. Wei, 2016, A physical modeling study of seismic features of karst cave reservoirs in the Tarim Basin, China: Geophysics, **81**, no. 1, B31–B41, doi: 10.1190/geo2014-0548.1.
Zemanek, J., 1971, Beam behavior within the near field of a vibrating piston: The Journal of the Acoustical Society of America, **49**, 181–191, doi: 10.1121/1.1912316.